# Proceedings of the ASME 2019 International Technical Conference and Exhibition on Packaging and Integration of Electronic and Photonic Microsystems InterPACK2019

October 7-9, 2019, Anaheim, CA, USA

# IPACK2019-6307

# BOILING HEAT TRANSFER USING SPATIALLY-VARIANT AND UNIFORM MICROPOROUS **COATINGS**

### Quang N. Pham

Materials and Manufacturing Technology University of California, Irvine Irvine, CA, USA, 92697

#### **Bowen Shao**

Mechanical and Aerospace Engineering University of California, Irvine Irvine, CA, USA, 92697

#### **ABSTRACT**

Two-phase thermal management offers cooling performance enhancement by an order of magnitude higher than single-phase flow due to the latent heat associated with phase change. Among the modes of phase-change, boiling can effectively remove massive amounts of heat flux from the surface by employing structured or 3D microporous coatings to significantly enlarge the interfacial surface area for improved heat transfer rate as well as increase the number of potential sites for bubble nucleation and departure. The bubble dynamics during pool boiling are often considered to be essential in predicting heat transfer performance, causing it to be a field of significant interest. While prior investigations seek to modulate the bubble dynamics through either active (e.g., surfactants, electricity) or passive means (e.g., surface wettability, microstructures), the utilization of an ordered microporous architecture to instigate desirable liquid and vapor flow field has been limited. Here, we investigate the bubble dynamics using various spatial patterns of inverse opal channels to induce preferential heat and mass flow site in highly-interconnected microporous media. A fully-coated inverse opal surface demonstrates the intrinsic boiling effects of a uniform microporous coating, which exhibits 156% enhancement in heat transfer coefficient in comparison to the polished silicon surface. The boiling heat transfer performances of spatiallyvariant inverse opal channels significantly differ based on the pitch spacings between the microporous channels, which dictate the bubble coalescent behaviors and bubble departure characteristics. The elucidated boiling heat transfer performances will provide engineering guidance toward designing optimal two-phase thermal management devices.

**KEY WORDS:** pool boiling, inverse opals, bubble dynamics, 3D microporous media, surface wettability

## Youngjoon Suh

Mechanical and Aerospace Engineering University of California, Irvine Irvine, CA, USA, 92697

## **Yoonjin Won**

Mechanical and Aerospace Engineering University of California, Irvine Irvine, CA, USA, 92697

#### INTRODUCTION

The performance of boiling heat transfer involves multiple interplaying thermophysical parameters, which include but are not limited to surface wettability [1,2], structural porosity [3], and cavity dimensions [4]. While numerous studies investigate such fundamental structure-property relations through porous surface modifications, their ultimate aim is to enhance boiling performance by exploiting and manipulating bubble dynamics [5-7]. The systematic control of both hydraulic and vapor transport in boiling optimizes the competing mechanisms of liquid rewetting and bubble departure, respectively. That is, as a bubble nucleates and eventually departs from the surface, the bulk liquid from the pool reservoir replaces the area during which heat is transferred by transient conduction from the heater surface to the liquid, decreasing the surface temperature temporarily until another saturated vapor bubble nucleates. The ebullition cycle continues to maintain a minimum surface temperature and thus maximize the heat transfer coefficient (HTC).

The strategies for optimizing such bubble dynamics for enhanced boiling performance have been explored by using either active (i.e., electrowetting and surfactant) [8,9] or passive (i.e., heterogeneous surface wettability) [10] solid-liquid interface control that can facilitate both mechanisms of liquid rewetting and bubble departure. Other passive approaches seek to leverage the underlying thermal and hydraulic transport mechanisms by utilizing microporous architecture coating [11,12]. For instance, Liter and Kaviany [13] employs periodic conical microporous structures with randomly packed pores to separate liquid and vapor transport pathways for minimal counterflow resistance. Without rationally designing appropriate vapor and liquid flow-fields during pool boiling, the growing bubbles can quickly coalesce to form a vapor blanket

above the heater surface and prevent liquid rewetting. This induces the limit of the boiling heat transfer process known as the critical heat flux (CHF), where the boiling surface temperature  $T_{\rm wall}$  significantly and rapidly increase.

Despite various efforts to manipulate the liquid-vapor flow field in pool boiling, no known study has applied such hydrothermal principles using a three-dimensional microporous coating that possesses homogeneous pore characteristics. Here, we examine the pool boiling performance of microporous pattern arrays with varying spatial arrangements. The porous coating composes of metallic inverse opal (IO) structure, which exhibits a highly-interconnected matrix of monosized pores arranged in a crystalline packing [14]. The precise control over the uniform pore distribution and porosity allows us to make accurate structure-performance correlations. The pitch spacings between porous regions as well as the porous coverage density are varied to examine bubble nucleation and boiling behaviors. The boiling performances of the spatially-varying porous regions are compared to those of a uniformly IO coating as well as a reference polished silicon surface to obtain the enhancement contribution through bubble dynamics control. The results from this investigation will provide significant insights toward optimizing the liquid-vapor flow field for enhanced boiling performance using rationally designed porous coatings.

#### **METHODS**

#### **Inverse Opal Preparation**

Spatially patterned nickel IOs are fabricated using colloidal template-assisted and selective template removal processes. The working surface is prepared by evaporating chromium (t =30 nm) and gold (t = 70 nm) onto a silicon substrate. Afterward, the silicon substrate is flipped to evaporate chromium (t = 30nm) and copper ( $t = 1 \mu m$ ) onto its underside, which improves the mounting contact adhesion with the copper heater. The gold-coated working surface is functionalized in 1 mM of aqueous sodium 3-mercapto-1-propanesulfonate for 24 h to render the surface hydrophilic. A colloidal suspension of monodispersed polystyrene spheres (4% in concentration and 0.6 µm in sphere diameter) is dropcasted onto the gold surface in an oven (Lab Line) at 70°C. As the solvent evaporates, the polystyrene spheres self-assemble into a close-packed colloidal structure, often known as an opal [15]. The opal template is annealed in an oven at 95°C for 3 h to increase the sphere-tosphere contact area as well as control the structural porosity [16]. To spatially pattern the opal template, the sample is mounted onto a 3-axis micrometer stage. A mounted capillary tube (< 0.5 mm in diameter) acts a miller and is lowered until it comes in contact with the opal surface, which is secured onto the micrometer stage to prevent perturbation. Due to the relatively weak adhesion forces between the polystyrene spheres and the gold surface, the packed spheres can be easily removed. The sample is then maneuvered with the micrometer stage to manually and selectively remove regions of the opal template with precisions to the desired pitch spacing  $\lambda$  and maintain the porous region width  $\gamma$ . Nickel subsequently infiltrates into the void spacings between the spheres through an electrodeposition process with an effective current density

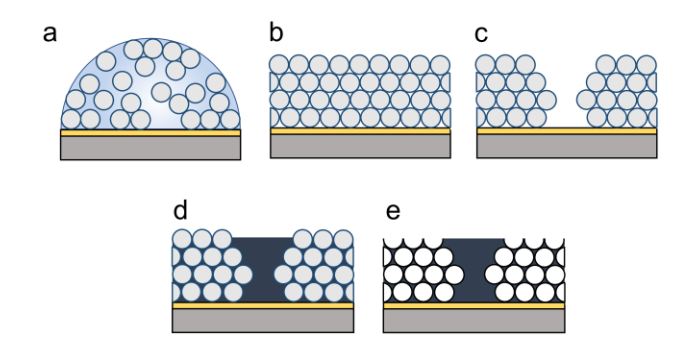


**Fig. 1** Schematics of Spatially Patterned Nickel Inverse Opal (IO) Preparation. a) A colloidal suspension of polystyrene spheres is dropcasted onto a gold-coated silicon substrate. b) The evaporation of the solvent causes the microspheres to self-assemble into a close-packed opal structure, and subsequent sintering of the opal film causes spheres to increase in contact areas. c) A micrometer stage is used to manually "mills" out the selective opal regions to create spatial patterns. d) Nickel electrodeposits into the interstitial spacings between spheres e) followed by a chemical removal of the polystyrene spheres to result in an IO structure.

of 1.5 mA/cm<sup>2</sup> in galvanostatic mode. In a three-electrode setup, the patterned opal template (working electrode) and a large nickel plate (counter electrode) are positioned ~2 cm apart in an aqueous electrolyte solution of 1M NiSO<sub>4</sub> + 0.2M NiCl<sub>2</sub> + 0.6M H<sub>3</sub>BO<sub>3</sub> while a Ag/AgCl serves as a reference electrode. To prevent nickel electrodeposition on the copper-coated underside of the silicon substrate, a lacquer coats the conductive surface area before the electrodeposition process. The resulting nickel-polystyrene composite structure immerses in a bath of tetrahydrofuran for a minimal of 12 h to dissolve the sacrificial polystyrene spheres, revealing regions of highly-porous nickel scaffold deemed as IO as well as regions of non-porous nickel manifested from the selectively removed opals. The lacquer coating on the substrate underside is simultaneously removed during the immersion in the tetrahydrofuran bath. The porous sample is rinsed with acetone, isopropanol alcohol, and deionized (DI) water. Due to surface contamination due to the ambient environment, the sample is cleaned in a 5% HCl aqueous solution for 2 min immediately before contact angle and pool boiling measurements.

## Surface Wettability Measurement

Water contact angle measurements provide insights toward the surface wettability of the spatially patterned nickel IOs. A goniometer (Kyowa Interface Science MCA-6) pneumatically dispenses ~15 nL of DI water onto both the IO and non-porous surfaces to measure the droplet contact angle. Measurements are conducted at room temperature with ~50% relative humidity. A high-speed camera (Photron Fastcam SA8) captures the droplet discharge at 1,000 fps, and an embedded software (FAMAS) fits the droplet profile using half-angle method to quantify the evolution of the contact angle. The apparent contact angles are measured through sessile drop method, and the dynamic contact angles are measured by

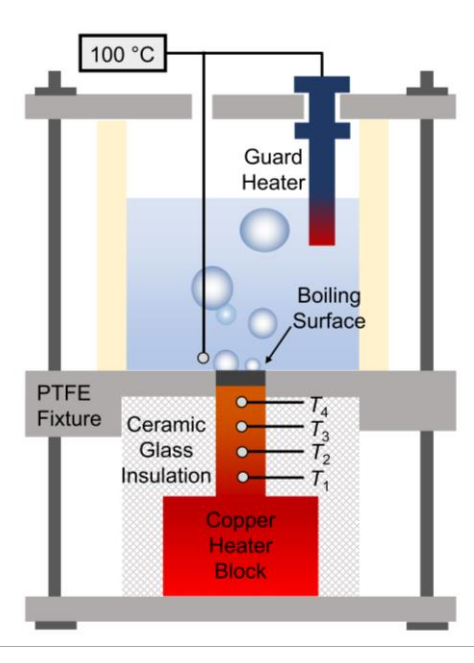


**Fig. 2** Schematic of Pool Boiling Measurement Apparatus. Cartridge heaters encapsulated in a monolithic copper block introduce a heat flux through the conductive medium toward the boiling surface. Ceramic glass insulation surrounding the copper block facilitates one-dimensional thermal conduction with minimal heat losses. The temperature gradients of the heat flux are monitored through four K-type thermocouples (*T*<sub>1</sub>-*T*<sub>4</sub>). A guard heater is connected to a thermocouple that is positioned slightly above the boiling surface through a PID controller, which is used maintain the saturated liquid pool at 100°C. A clear boiling chamber provides direct visualization of bubble dynamics as captured by a high-speed camera (not shown).

increasing and decreasing the droplet volume to determine the advancing and receding contact angles, respectively.

#### **Pool Boiling Measurement**

Nucleate pool boiling heat transfer of nickel IO coated surfaces is experimentally investigated with varying pitch spacing between porous regions. DI water serves as the working fluid, which is degassed through continuous boiling for ~30 min before experiments. At the base of the boiling apparatus (see Fig. 2), four cylindrical cartridge heaters (Omega, CIR-2015) controlled by an AC voltage regulator (Variac Transformer) heat an encompassing copper block to transport a heat flux toward the sample. By modulating the electric power supply through the cartridge heaters at the base, the applied heat flux of the copper block can be slowly increased. An insulating ceramic fiber blanket encloses the heating copper block to promote one-dimensional thermal conduction and reduce heat losses. Four K-type thermocouples are incrementally positioned along the heating copper block and directly below the boiling surface to determine the temperature gradient and thus calculate the boiling surface temperature  $T_{\text{wall}}$  and the heat flux  $q''=-k\Delta T/L$ , where k is the thermal conductivity of the copper block,  $\Delta T$  is the temperature difference measured between a prescribed distance L. At each applied heat flux, temperatures are monitored through a linked data acquisition

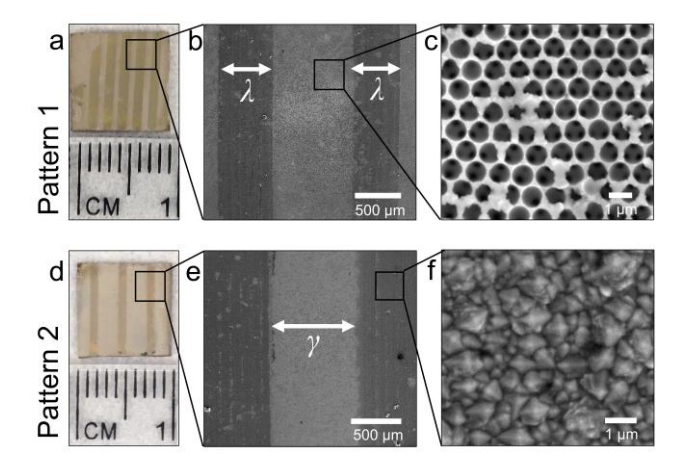
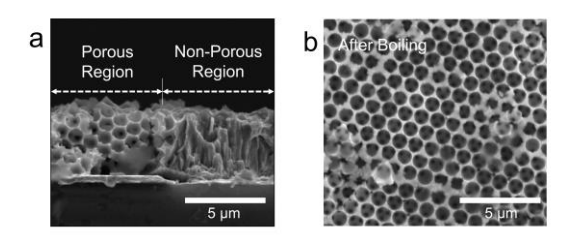


**Fig. 3** Nickel IOs with Spatial Varying Geometries. Optical images of the samples denoted as Pattern 1 and Pattern 2 are shown in a,d), respectively, companied with b,e) associated top view scanning electron microscopy (SEM) images show the overviewing microporous patterns. c) A representative detailed SEM image of the microporous architecture displays uniform pore distributions and high interconnectivity. f) Representative SEM image of the non-porous nickel region shows nanoscale roughness from the electrodeposited nickel crystals.

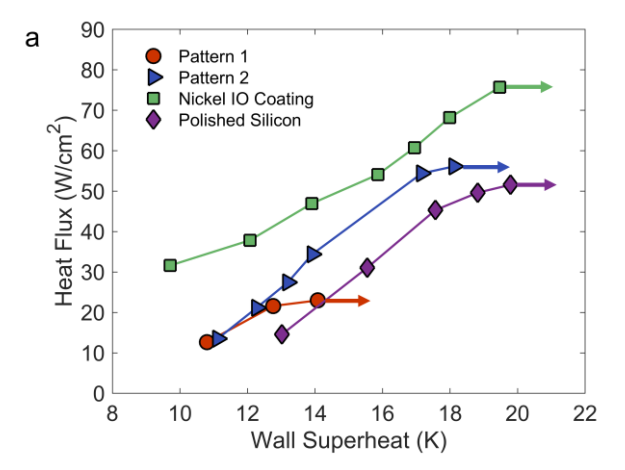
system (LabJack U6) and recorded during steady state to produce the boiling curves. More details regarding heat flux calculations are provided in prior work [17]. A clear boiling chamber is used to allow visual monitoring of nucleating bubble dynamics. A high-speed camera (FASTCAM Mini AX50) captures the dynamics of bubble nucleation and departure at 2,000 fps through the transparent wall of the boiling chamber. A thermocouple located slightly above the boiling surface is connected to a guard heater through a PID controller, which ensures that the pool liquid temperature remains saturated. The accuracy of the K type thermocouple is within  $\pm$  1.1 °C. The maximum uncertainties of heat flux and HTC are expected to be  $\pm$  7.3 W/m² and  $\pm$  10.3 °C, respectively.

#### RESULT AND DISCUSSIONS

The resulting nickel IOs with discretized porous channels are displayed in Fig. 3, denoted as Pattern 1 and Pattern 2. The porous channels can be seen as the darker colored regions through optical images. Scanning electron microscopy (SEM)



**Fig. 4** Nickel IOs after Boiling. a) Cross-sectional SEM image of the microporous and non-porous nickel channels. b) Top view SEM of Pattern 1 after reaching boiling CHF, showing limited structural changes.



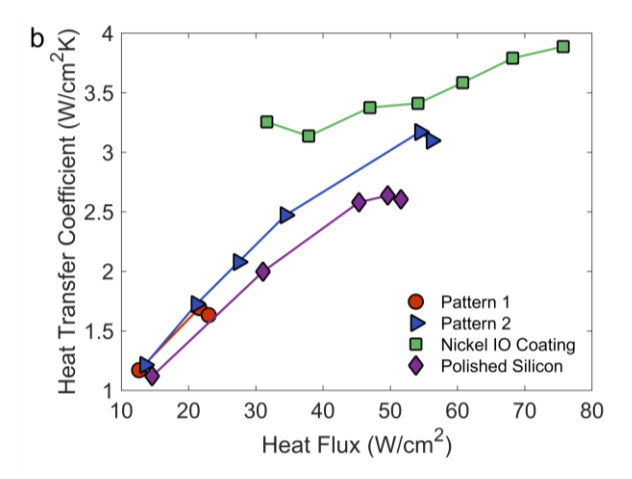


**Fig. 5** Pool Boiling Performance Results. a) The heat flux plotted in relation to the wall superheat until critical heat flux (CHF) is reached as indicated by the arrows. In comparison to the polished silicon, the Pattern 1 sample improves heat transfer performance with lower wall superheat temperatures. Pattern 2 sample exhibits the poorest boiling performance while the uniform coating of nickel inverse opal performs the best. b) The heat transfer coefficients (HTCs) of all samples increase with increasing heat flux.

images provide detailed views of the microporous architecture, which exhibits uniform pore distributions and highlyinterconnected networks. The non-porous nickel regions show nanoscopic roughnesses contributed by the electrodeposited nickel crystals. Both Pattern 1 and Pattern 2 possess a constant porous region width  $\gamma$  of 1.0 mm with varying pitch spacings  $\lambda$ of 1.5 and 3.0 mm, respectively. Both patterned porous samples have a structural thickness  $\delta$  of 4.5 um, as confirmed with crosssectional SEM after the boiling experiment in Fig. 4a. The cross-sectional view of the sample also displays the conjunction between the microporous and non-porous nickel channels. All porous samples possess pore diameter  $d_p$  of  $0.579 \pm 0.019 \,\mu\text{m}$ . The structural porosity of the nickel IOs remains constant at ~78% for Pattern 1, Pattern 2, and fully-coated IO (referred to as "nickel IO coating" or "nickel IO" in figures). The porosity  $\phi$  of IOs is calculated using an expression derived from computation fluid dynamics [16]:  $\phi = 0.5833(d_v/d_p) + 0.6633$ , where  $d_v$  is the diameter of the interconnected window between spherical pores.

Immediately before subjecting the samples to boiling conditions, they are cleaned by rinsing in diluted 5% HCl to remove hydrocarbon adsorption and oxidation that are typical for surfaces exposed to ambient environment. Before boiling, the nickel IOs and nickel nonporous regions possess apparent contact angles of ~30°, suggesting a hydrophilic surface. However, as we previously demonstrated that during the boiling process, the hydrophilic surface rapidly becomes hydrophobic within minutes possibly due to oxidation [17]. This suggests that the examined nickel-based surfaces should be considered hydrophobic during the entirety of the boiling experiment. The silicon surface is also hydrophobic with apparent, advancing, receding contact angles of  $99.9^{\circ} \pm 0.9^{\circ}$ ,  $97.4^{\circ} \pm 6.7^{\circ}$ , and  $38.8^{\circ} \pm 9.7^{\circ}$ , respectively.

Despite the surface chemistry of the nickel microstructure changing due to boiling, the porous architecture of the nickel-based IO withstands the extreme effects of boiling as seen through the relatively unchanged structural features after boiling (see Fig. 4). This significantly contrasts with using copper as the boiling surface in a previous study [4], which is shown to be highly-oxidative with structural damages. The limited oxidative states of nickel suggest it as a potentially durable boiling surface.

The boiling curves of spatially-variant IOs, fully-coated IOs, and polished silicon are plotted in Fig. 5a as a function of wall superheat ( $\Delta T = T_{\text{wall}} - T_{\text{sat}}$ ) until CHF is reached. Pattern 2 exhibits slightly better boiling performance than the referenced bare silicon surface with CHFs of 56.1 W/cm² compared to 51.6 W/cm². Pattern 2 also consistently possess higher HTCs for a given heat flux than the polished silicon surface (see Fig. 5b). The fully-coated nickel IO demonstrate the best heat transfer performance with the highest CHF value of 75.7 W/cm² and 156% enhancement in HTC compared to smooth silicon. Conversely, Pattern 1 shows the poorest boiling performance by quickly approaching CHF at 23.0 W/cm².

Among the four examined surfaces, they all possess similar surface energies (i.e., nonwetting). The variations among them are the nucleation site densities, heat transfer surface areas, and nonporous region spacings between porous channels. The superior boiling performance of the fully-coated IO may be attributed to its large aerial density of cavities for the highest number of bubble nucleation sites and highest interfacial heat transfer areas compared to the remaining samples. However, Pattern 1 possesses approximately 41% more in porous surface areas than Pattern 2 despite performing the poorest, suggesting that porous area coverage is not entirely sufficient in dictating the heat transfer efficacy especially when intervals of porous regions are spatially controlled.

In spatially-variant porous channels, the homogeneous hydrophobicity between both the IO and non-porous regions is likely to promote bubble nucleation and departure with limited liquid rewetting functionality. That is, the nanoscopic roughness from the nickel non-porous regions shown in Fig. 3f can also contribute to bubble nucleation, but the bubble growth rate on the non-porous regions may be slower in comparison to that at the IO channels due to less available vapor-filled cavities. Therefore, Pattern 1 may have higher aerial coverage

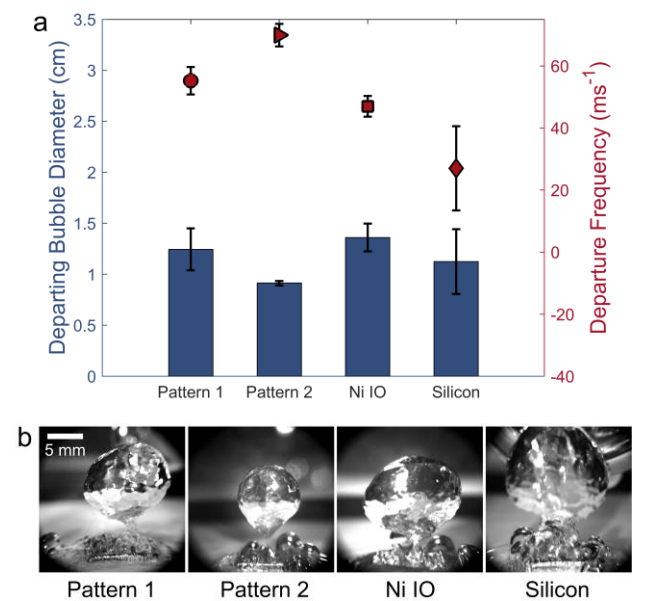


**Fig. 6** Departing Bubble Characteristics. A high-speed camera captures the bubble formations with increasing heat fluxes. a) At critical heat flux, the diameters of the departing bubbles and their departure frequencies are shown in blue bars and red scatter points, respectively. b) Representative high-speed camera captures of the departing bubbles that correspond to different surface coatings.

of porous region than Pattern 2, but the smaller pitch spacing  $\lambda$  between IO channels for Pattern 1 may promote the bubbles to quickly coalesce near the boiling surface and form a vapor blanket. Conversely, the IO channels of Pattern 2 are further separated, minimizing the chances of vapor film formation before bubble departure occurs.

The departing bubble diameters and frequency are plotted in Fig. 6 at the associated CHFs for each boiling surface, showing that polished silicon surface exhibit the largest variations in bubble diameters and departure frequencies. Representative high-speed camera captures of bubble characteristics at CHF (Fig. 6b) show that Pattern 1 nucleate smaller bubbles that coalesce at the boiling surface until a sufficiently large bubble overcomes the effect buoyancy and depart from the surface.

## **CONCLUSION**

The boiling heat transfer of spatially-variant microporous channels and complete coverage of microporous coatings with uniform pore distribution demonstrates the significant effects of surface wettability on controlling bubble dynamics for enhanced cooling performance. Here, fully-coated IOs exhibit the best boiling heat transfer performance due to its enormous nucleation site density through the interconnected cavities. However, despite Pattern 1 possessing larger porous surface areas than Pattern 2, the smaller pitch spacing in Pattern 1 causes bubbles to quickly coalesce on the boiling surface and reach CHF earlier. In addition, the homogeneous hydrophobicity between the porous and nonporous regions prevents the liquid from rewetting the surfaces. In future work, the evaporation of silica onto the nonporous regions will

provide heterogeneous surface wettability while preserving the designated bubble nucleation sites along the IO channels, which may facilitate an ordered flow field of surface rewetting and bubble departure. While the optimization of pitch spacings between the patterned microporous channels is outside the scope of this work, it should be noted that tuning the wavelength to coincide with the capillary length can enhance the HTC and CHF. The initial finding from this investigation underscores the importance of the rationally designed liquid-vapor flow field in boiling heat transfer of spatially-variant microporous channels.

#### **ACKNOWLEDGEMENT**

This work was sponsored by the National Science Foundation (NSF), (CBET-TTP 1643347, Dr. Jose Lage, the Program Director, Thermal Transport Processes). SEM imaging was performed using instrumentation funded in part by the National Science Foundation Center for Chemistry at the Space-Time Limit (CHE-0802913).

#### REFERENCES

- [1] O'Hanley, H.; Coyle, C.; Buongiorno, J.; McKrell, T.; Hu, L.-W.; Rubner, M.; Cohen, R. Separate Effects of Surface Roughness, Wettability, and Porosity on the Boiling Critical Heat Flux. *App. Phys. Lett.* 2013, 103, 024102.
- [2] Nam, Y.; Wu, J.; Warrier, G.; Ju, Y. S. Experimental and Numerical Study of Single Bubble Dynamics on a Hydrophobic Surface. *J. Heat Transfer* 2009, 131, 121004.
- [3] Zhang, C.; Palko, J. W.; Barako, M. T.; Asheghi, M.; Santiago, J. G.; Goodson, K. E. Enhanced Capillary-Fed Boiling in Copper Inverse Opals via Template Sintering. Adv. Funct. Mat. 2018, 1803689.
- [4] Pham, Q. N.; Zhang, S.; Cheng-Hui, L.; Hao, S.; Won, Y. Boiling Heat Transfer Performance of Threedimensionally Ordered Microporous Copper with Modulated Pore Diameter. 2018 17th IEEE Intersociety Conference on Thermal and Thermomechanical Phenomena in Electronic Systems (ITherm), San Diego, CA, 2018, 1-6.
- [5] Thome, J. R. Boiling in Microchannels: A Review of Experiment and Theory. *Int. J. Heat Fluid Flow* 2004, 25, 128–139.
- [6] Cooke, D.; Kandlikar, S. G. Pool Boiling Heat Transfer and Bubble Dynamics over Plain and Enhanced Microchannels. J. Heat Transfer 2011, 133, 052902.
- [7] Thiagarajan, S. J.; Yang, R.; King, C.; Narumanchi, S. Bubble Dynamics and Nucleate Pool Boiling Heat Transfer on Microporous Copper Surfaces. *Int. J. Heat Mass Transfer* 2015, 89, 1297-1315.
- [8] Xu, H.; Yan, R.; Wang, S.; Chen, C.-L. Bubble Detachment Assisted by Electrowetting-Driven Interfacial Wave. *Physics on Fluids* 2017, 29, 102105.
- [9] Cho, H. J.; Mizerak, J. P.; Wang, E. N. Turning Bubbles On and Off During Boiling Using Charged Surfactants. *Nat. Comm.* 2015, 6, 8599.

- [10] Rahman, M. M.; Pollack, J.; McCarthy, M. Increasing Boiling Heat Transfer using Low Conductivity Materials. *Sci. Rep.* 2015, 5, 13145.
- [11] Kandlikar, S. G. Controlling Bubble Motion Over Heated Surface through Evaporation Momentum Force to Enhance Pool Boiling Heat Transfer. *App. Phys. Lett.* 2013, 102, 051611–051615.
- [12] Dhillon, N. S.; Buongiorno, J.; Varanas, K. K. Critical Heat Flux Maxima During Boiling Crisis on Textured Surfaces. *Nat. Comm.* 2015, 6, 8247.
- [13] Liter, S. G.; Kaviany, M. Pool-Boiling CHF Enhancement by Modulated Porous-Layer Coating: Theory and Experiment. *Int. J. Heat Mass Transfer* 2001, 44, 4287-4311.
- [14] Pham, Q. N.; Barako, M. T.; Tice, J.; Won, Y. Microscale Liquid Transport in Polycrystalline Inverse Opals across Grain Boundaries. *Sci. Rep.* 2017, 7, 10465.
- [15] Suh, Y.; Pham, Q. N.; Shao, B.; Won, Y. The Control of Colloidal Grain Boundaries through Evaporative Vertical Self-Assembly. *Small* 2019, 15, 1804523.
- [16] Pham, Q. N.; Shao, B.; Kim, Y.; Won, Y. Hierarchical and Well-ordered Porous Copper for Liquid Transport Properties Control. ACS App. Mat. Interfaces 2018, 10, 16015-16023.
- [17] Pham, Q. N.; Zhang, S.; Hao, S.; Won, Y. Boiling Heat Transfer with Well-Ordered Microporous Architecture. *ACS App. Mat. Interfaces* 2019 (under review).